PHOTOMETRIC PARAMETER MAPS OF THE MOON FROM LROC WAC OBSERVATIONS. H. Sato[1], B. W. Denevi[2], M. S. Robinson[1], B. W. Hapke[3], A. S. McEwen[4], LROC Science Operation Team[1], [1]Arizona State University, 1100 S. Cady Mall, INTDS A120A, Tempe, AZ 85287-3603 (hsato@ser.asu.edu), [2]Applied Physics Lab., Johns Hopkins University, Laurel, MD, [3]University of Pittsburgh, Pittsburgh, PA, [4]University of Arizona, Tucson, AZ.

Introduction: The Lunar Reconnaissance Orbiter (LRO) Wide Angle Camera (WAC) acquires monthly near-global coverage [1], and each month presents a unique set of imaging geometries (incidence (*i*), emission (*e*), phase (*g*) angles). Due to the WAC's wide field-of-view (60° in 7-color mode), images are taken with a wide variation of *e* and *g* across track. By combining these monthly observations we derive spatially resolved Hapke photometric parameters [2]. Since the photometric properties are linked to various soil properties such as albedo, grain size, and shape [2,3,4], derived parameter maps are useful for assessing surface properties as well as photometric normalization.

Using a tile-by-tile method [5], we derived Hapke parameters for each 2° (~60.6 km) tile between ±70° latitude, and for each 0.05° (~1516 m) tile for a smaller sample area near the Apollo 17 landing site. Within the five parameters of simplified Hapke function (*w*, *b*, *c*, B_{C0}, and *hc*) [6], we focused on *hc* (inverse of transport mean free pass in the medium), *b,* and *c* (the Henley-Greenstein (H-G) double lobe parameters), which systematically vary with grain shapes and opacities [2,3,4]. From these maps, we investigate the correlation between geologic units and photometric properties.

Methodology: About 66,000 WAC images acquired from February 2010 to October 2011 were radiometrically corrected, partitioned into gridded tiles, and stacked in a time series (tile-by-tile method [5]). Viewing parameters (*i*, *e*, *g*) were computed using the WAC digital terrain model (100 m/pixel) [7]. Next the simplified Hapke function [6] photometric parameters were calculated by curve fitting with the Levenberg-Marquardt least-squares algorithm [8]. Since this algorithm cannot find a unique global minimum, the starting value can affect the result. To avoid this problem, we used 50 randomly generated parameter sets as the starting values, and for each starting value, we calculated the best-fit parameter set and the fitting error (sum of the difference between the I/F and modeled values). Then we selected the parameter set with minimum fitting error. Approximately 50% of the fitting results returned identical values with minimum fitting error, thus there is a high probability that the calculated values are the global minimum.

Results: Narrow vertical zones at longitude 80+/-5°E and 260+/-5°E (enclosed by dashed line in Fig.1) show systematically high *b* and *c*, as well as low *hc* values and correspond to regions of low data density (about 4 times fewer WAC images than the others), which resulted in reduced fitting accuracy. These areas contain a paucity of image data as the camera is disabled during monthly burns, which occur in these two narrow longitude bands.

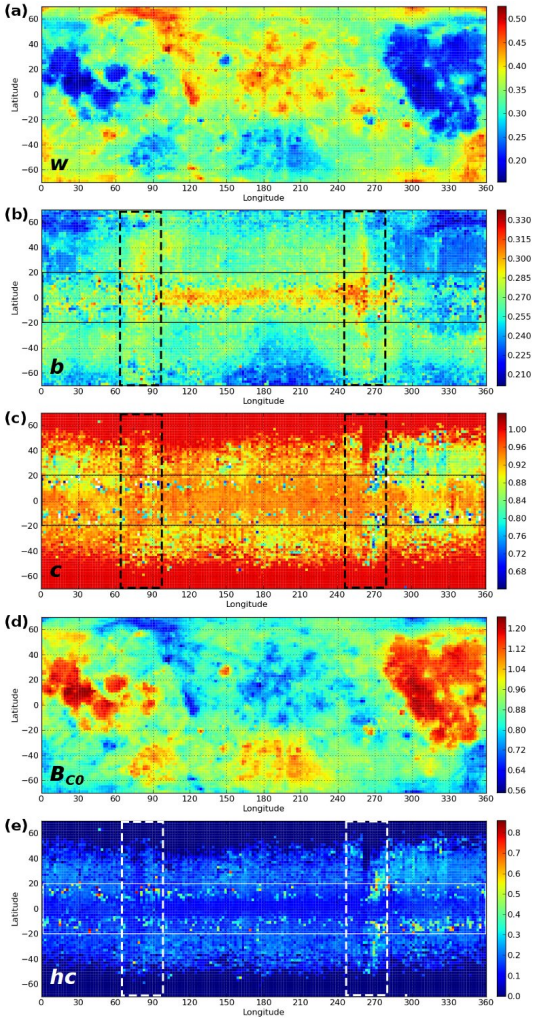

Fig.1 Global photometric parameter maps (0~360°E, -70~70°N) with 2by2 degree tiles. Single scattering albedo:*w* (a), double lobed H-G parameter: *b* (b), *c* (c), amplitude of coherent backscatter opposition surge effect: B_{C0} (d), inversed parameter of transport mean free path in the medium as a function of wavelength: *hc* (e) of 604 [nm] band are shown in linear stretched colors. Note that minimum and maximum values do not correspond to the color bar range.

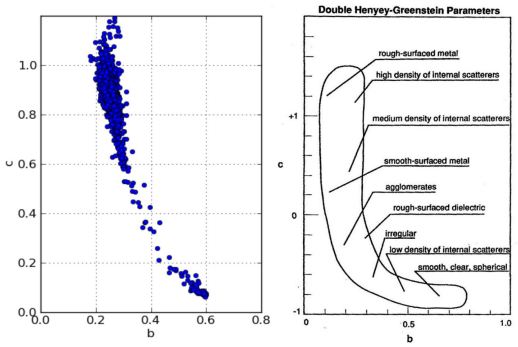

Fig.2 Plot of *b* and *c* of 604 [nm] band (left) in 0.05° tile parameter map shown in Fig.3, and expected grain properties from *b*-*c* relationship (right), from Hapke (1993) p.122, Fig.6.9. Note that the range 0~1 of *c* at left plot corresponds to -1~1 of *c* in right plot, due to the H-G function's expression difference.

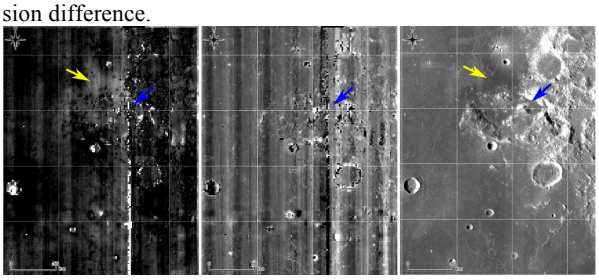

Fig.3 0.05°(~1516 m) tile parameter maps of *b*(left) and *c*(middle) at lat:14~23°N, lon:26~33E° of 604 [nm] band. LROC WAC 100 m/pixel monochrome mosaic of same area is shown in right. Blue and yellow arrows indicate Apollo 17 landing site and the high *b* value area respectively. Grid lines are inserted in every 2°.

The parameter map for *w*, the single scattering albedo (Fig.1a), strongly corresponds to the surface albedo as expected. At high latitudes where no low-phase observations are available, B_{C0} (amplitude of coherent backscatter opposition surge effect) is calculated based on the negative correlation between B_{C0} and *w* observed at the equator [9]. Thus B_{C0} (Fig.1d) is essentially an inverse of surface albedo *w*. The parameters *b* (Fig.1b), *c* (Fig.1c) and *hc* (Fig.1e) are systematically high or low between latitude +/- 10° to 15° (enclosed by narrow solid line in Fig.1), especially in the farside highlands.

The correlation between *b* and *c* is controlled by the optical properties of surface materials [2,3,4]. As shown in Fig. 2 (right), as grains vary from those with rough surface and moderate density like agglutinates or scoria to grains with smooth surfaces like glassy materials, *b* increases and *c* decreases. To investigate this further we examined 0.05° (~1516 m) tile parameter map calculated for the Apollo17 landing site (Fig.3). According to laboratory experiments [3,4], plots of *b* and *c* (Fig. 2, left) correspond to the materials from round shaped opaque, rough-surface to irregular shaped translucent, rough-surface properties.

In the 0.05° parameter map of *b* (Fig. 3, left) for the Apollo17 landing site region, relatively high values for *b* can be recognized along the dark mantle deposits [10]. However artifacts in the parameter map of *c* make it difficult to interpret, especially in regions of high topographic variation.

Discussion: The equatorial zone seen in the parameter maps *b, c* and *hc* (in Fig.1 b, c, e) at 604 nm is also detected in all other filters, as well as when a single-lobed H-G function is employed. One potential cause of this zone is the lack of low-phase observations at high latitudes; observations critical for the determination of *b*, *c*, and B_{C0}. The interpolation of B_{C0} at high latitudes [9] is based on *w* and B_{C0} between 4°S and 4°N latitudes, much narrower range than the observed anomalous equatorial zone in *b*, *c* and *hc*, thus we do not believe this zone is the result of our B_{C0} interpolation procedure. If the difference between equatorial and high-latitude photometric properties is not an artifact of poor phase coverage at high latitudes, the equatorial materials may be optically isolated from those at high latitudes. Further spatial comparisons using various data sets (e.g. spectral/thermal/radar) could help to confirm the existence of this anomalous equatorial region.

In the Apollo 17 region (Fig. 3), the relatively high value of *b* for the dark mantle deposits is consistent with values expected for pyroclastic glasses. However, noise and artifacts that remain in the parameter map of *c* (Fig.3, right), which are likely due to poor fits for emission angle or errors in the radiometric calibration. The phase function at each tile is based on about 1500~2000 data points from more than 10 images. For tiles smaller than 1°, emission and incidence angles are biased due to the small orbital shifts of LRO at each month and low data density within each tile. Improvements to the radiometric calibration, especially the flatfield and potential temperature sensitivity effects, and increased fitting accuracy are required. Also adding more images over time will increase emission and incidence angle variations thus reducing artifacts.

References: [1] Robinson M. S. et al. (2010) *Space Sci. Rev., 150*, 81-124. [2] Hapke B. (1993) *Cambridge Univ. Press*, New York. [3] McGuire A. F. and Hapke B. (1995) *Icarus 113*, 134-155. [4] Souchon et al. (2011) *Icarus 215*, p313-331. [5] Sato H. et al. (2011) *LPS XXXXII*, Abstract #1974. [6] Hapke B. et al. (2012) *JGR,* in press. [7] Scholten F. et al. (2011) *LPS XXXXII*, Abstract #2046. [8] Philip E. G. and Murray W. (1978) *SIAM J. Numerical Analysis 15*, 5, 977-992. [9] Sato H. et al. (2011) *EPSC-DPS*, Abstract #EPSC-DPS2011-636. [10] Hawke B. R. and Coombs C. R. (1994) Proceedings of ECOS IV, pp 1008-1019.